GDCh Research Article Angewandte International Edition Chemie www.angewandte.org

How to cite: *Angew. Chem. Int. Ed.* **2025**, e202512780
doi.org/10.1002/anie.202512780

Zinc Metal Batteries

Dienoic-Acid Coupling Effect Induced Hierarchical Interface for High-Performance Zinc Metal Batteries

Tianyi Yang, Tingting Su, Mi Xu, Dongdong Wang, Wenfeng Ren,* Haozhen Dou,* Runcang Sun, and Zhongwei Chen**

Abstract: Rational pre-design of self-decomposed electrolyte additives to construct solid electrolyte interphase (SEI) for suppressing hydrogen evolution reaction (HER) and dendrite growth of zinc (Zn) anode confronts enormous challenges, especially for the in-depth understanding of structure–function relationship and the lack of reasonable design criteria. In this work, the dienoic-acid coupling effect is innovatively proposed to in-situ construct a hierarchical SEI layer (HSL) through the structural screening of a series of organic-acid molecules. Strong electron-withdrawing ability of dual carboxyl and metastable double bond can strengthen the self-decomposition tendency of trace electrolyte additive to form HSL via chemical and electrochemical reaction. HSL can effectively regulate interfacial H_2O environment via hydrogen-bond anchoring to reduce thermodynamically active H_2O, facilitate desolvation kinetics, and uniform Zn^{2+} diffusion, thus significantly suppressing HER and dendrite growth. As a result, Zn anode with HSL can achieve high average coulombic efficiency of 99.8% over 2400 cycles, long-term cycling stability of 3800 h, and good reversibility under 50 mA cm^{-2}. Zn–I_2 full battery with HSL displays a long cycling life of 15 000 cycles and successfully powers the portable and wearable instruments. This work opens a novel route to design an advanced interface with fast kinetics by trace electrolyte additive for high-performance Zn metal batteries.

Introduction

Aqueous zinc (Zn) metal batteries with high safety and low cost are increasingly recognized as a promising candidate for energy storage. Zn metal is a promising anode material owing to its high theoretical capacity (5855 mAh cm^{-3}, 820 mAh g^{-1}) and moderate redox potential (−0.76 V vs. SHE).[1,2] However, the fundamental challenges of hydrogen evolution reaction (HER) and dendrite growth associated with Zn anode significantly deteriorate the electrochemical performance of Zn metal batteries, which is mainly caused by interfacial active H_2O and disturbed Zn^{2+} flux within the electric double layer.[3] Thermodynamically active H_2O induces severe HER to generate hydrogen and insulative by-product, the uneven Zn^{2+} diffusion favors generating dendrite growth,[4] and the slow desolvation process of Zn^{2+} results in the reduced redox kinetics with high polarization potential.[5–8] Various approaches, such as electrolyte engineering,[9–11] separator development,[12] and electrode modification,[13] have been developed to address the aforementioned challenges, yielding improvements in electrochemical performance.

Interface engineering has emerged as a highly effective strategy to address the above challenges of Zn metal anodes via the construction of highly reversible interfaces,[14,15] mainly including the development of strongly adsorbed molecular layer,[16] the construction of artificial protective layer,[17,15] and the design of solid electrolyte interfaces (SEI) layer.[18] Comparatively, the in situ construction of the SEI layer is a more effective methodology to shield interfacial active H_2O and regulate Zn^{2+} deposition behavior compared with the above two strategies, as well as an easy scale-up and high economic approach.[19,20] Among various SEI, the hierarchical SEI layer with organic/inorganic components stands out by combining the advantages of both organic-rich layer and inorganic-rich layer.[21] The organic-rich outer layer imparts the flexibility, the modulation of interfacial H_2O, and the desolvation kinetics of Zn^{2+}, while the inorganic-rich inner layer exhibits high ionic conductivity to facilitate uniform ion diffusion and mitigate dendrite formation. At present, the construction of hierarchical SEI layer mainly relies on the adsorption behavior as well as co-decomposition of organic solvent and/or anion through the frequent requirement of high-concentrated organic solvent and Zn salt in aqueous electrolyte, which sacrifices the battery safety and causes sluggish interface kinetics. Therefore, the

[*] T. Yang, T. Su, Prof. W. Ren, Prof. R. Sun
Liaoning Key Laboratory of Lignocellulose Chemistry and BioMaterials, Liaoning Collaborative Innovation Center for Lignocellulosic Biorefinery, College of Light Industry and Chemical Engineering, Dalian Polytechnic University, Dalian 116034, China
E-mail: tingting_su1988@yeah.net
wfren@dlpu.edu.cn

M. Xu, D. Wang, Prof. H. Dou, Prof. Z. Chen
State Key Laboratory of Catalysis, Dalian Institute of Chemical Physics, Chinese Academy of Sciences, Dalian 116023, China
E-mail: haozhen@dicp.ac.cn
zhwchen@uwaterloo.ca

Prof. W. Ren, Prof. H. Dou, Prof. R. Sun, Prof. Z. Chen
Yulin Innovation Institute of Clean Energy, Yulin 719053, China

Additional supporting information can be found online in the Supporting Information section

construction of a hierarchical SEI layer by trace electrolyte additives without compromising safety and kinetics is highly desired yet confronts an enormous challenge, especially for the structure design of electrolyte additives. Moreover, the in-depth mechanism of pre-designed decomposition regulation is far away understood.

Herein, the dienoic-acid coupling effect was discovered through the structural screening of a series of dicarboxylic-acid molecules. An electrolyte additive design strategy based on dienoic-acid coupling effect was proposed to effectively construct a hierarchical SEI layer (HSL) via the electron-withdrawing ability of dual carboxyl and metastable double bond, which can obviously reduce the electron energy barrier and regulate the electron structure of α carbon in dual carboxyl groups. As a proof of concept, the dienoic-acid coupling effect of fumarate salt as a trace electrolyte additive facilitates the self-decomposition reaction to form HSL with the organic outer layer and the inorganic inner layer on the Zn anode. The organic outer layer can effectively regulate the interfacial H_2O environment via the anchoring effect of hydrogen bonds to hinder HER, as well as facilitate the desolvation kinetics and the uniform ion diffusion to suppress dendrite growth. The inorganic inner layer possesses the fast ion-transport ability to uniform deposition behavior for further avoiding dendrite formation. As a result, HSL endows Zn anode with a high average coulombic efficiency of 99.8% over 2400 cycles, long-term cycling life of 3800 h, and good reversibility under high current density of 50 mA cm^{-2}. Moreover, Zn–I_2 full battery with HSL displays excellent cycling stability of 15 000 cycles for coin battery and 550 cycles for pouch battery, and successfully powers the portable and wearable instruments. This work aims to shed light on the design of advanced interfaces and the regulation of interfacial active H_2O for high-performance batteries via additive molecular engineering, as well as accelerate the practical application of aqueous Zn metal batteries.

Results and Discussion

The self-decomposition of electrolyte additives is an effective route to in situ construct a solid electrolyte interphase (SEI) layer for suppressing the hydrogen evolution reaction (HER) and dendrite growth on zinc (Zn) anode, but confronts the in-depth understanding of structure–function relationship and the lack of reasonable design criteria. In this work, the dienoic-acid coupling effect is innovatively proposed by the combination of dual carboxyl and double bond groups to in situ construct a hierarchical SEI layer (HSL) with the organic outer layer and the inorganic inner layer. A series of organic-acid molecules was selected as trace electrolyte additives to investigate self-decomposition tendency by the calculation of the lowest unoccupied molecular orbital (LUMO) energy levels in Figure 1a. Fumarate acid, pentenedioic acid, and mesaconic acid with a double bond possess lower LUMO energy than those without a double bond (succinic acid, glutaric acid, and adipic acid), indicating that the presence of a double bond reduces the stability of organic acids and facilitates the occurrence of decomposition reactions. Moreover, their LUMO energy order of dual carboxyl organic acids with different carbon numbers is adipic acid, glutaric acid, and succinic acid, verifying that the increase of the middle carbon number can weaken the electron-withdrawing effect of the carboxyl group and reduce the self-decomposition tendency. Among these organic acids with dual carboxyl, fumarate acid possesses the optimal molecule structure of four carbon atoms, dual carboxyl, and a single double bond to own the lowest LUMO energy, which has a great tendency to undergo the preferential self-decomposition reaction.[22–24]

The self-decomposition mechanism of the dienoic-acid coupling effect is summarized and shown in Figure 1b. The conjugated system of fumarate acid enables the delocalization of electrons within fumarate acid molecule, in which the electron-withdrawing effect of the carboxyl group facilitates the accumulation of δ^+ charge on the α carbon. Subsequently, the electrons generated by electrode reduction are injected into the π antibonding orbitals of the double bond to destroy the delocalization structure, which causes the unpaired electron transformation into the α carbon and the formation of a radical anion intermediate (R—COO·$^-$).[25] At last, metastable R-COO·$^-$ induces the decarboxylation reaction to break the C—C bond and form CO_2,[26] as well as an inorganic $ZnCO_3$ component is produced by the mineralization reaction with Zn^{2+} with CO_2 on Zn anode. HSL can significantly reduce the interfacial active H_2O by anchoring free H_2O with hydrogen-bond (H-bond) networks (Figure 1c), facilitating the desolvation processes by the strong coordination with Zn^{2+} ions, and afford uniform deposition behavior by the homogeneous ion diffusion ability (Figure 1c).

The coordination adsorption behavior and the coupled reaction for the construction of the organic outer layer were investigated by density functional theory (DFT), X-ray photoelectron spectroscopy (XPS), and Fourier transform infrared spectroscopy (FTIR). The absorption energy of fumarate salt (FS) and H_2O on different Zn crystal planes to analyze the competitive adsorption behavior (Figure 2a). The adsorption energy of parallelly placed FS towards Zn(002) (−4.58 eV), Zn(100) (−5.10 eV), and Zn(101) (−4.18 eV) crystal planes for Zn anode is higher than the H_2O on Zn(002) (−0.33 eV), Zn(100) (−0.28 eV) and Zn(101) (−0.30 eV). In addition, the adsorption energy of FS in the parallel state is higher than that of FS in the vertical state to Zn(002) (−3.37 eV), Zn(100) (−3.95 eV), and Zn(101) (−3.27 eV) crystal plane, indicating that FS molecules are priority adsorbed on Zn surface in a parallel tendency.[27] The differential charge density in Figure S1 illustrates a larger overlapping electron cloud on the Zn surface via the double-ended carboxyl group electron-rich distribution of FS (Figure S2), thus creating stronger chemisorption.[28] In XPS spectra, the carbon (C) element was observed on the electrode surface after soaking (Figure S3). C 1s spectra (Figure 2b) show a noticeable decrease in the O-C=O signal, demonstrating the coordination of the O—C=O group with the Zn surface.[29] In O 1s spectra, the decrease in oxygen electron density leads to a peak shift of O—C=O from 531.4 to 531.6 eV,[30] resulting from the coordination effect to cause environmental change.[31] Compared with bare Zn, the enhanced characteristic peak intensity of FS on the Zn anode with HSL further confirms the successful construction

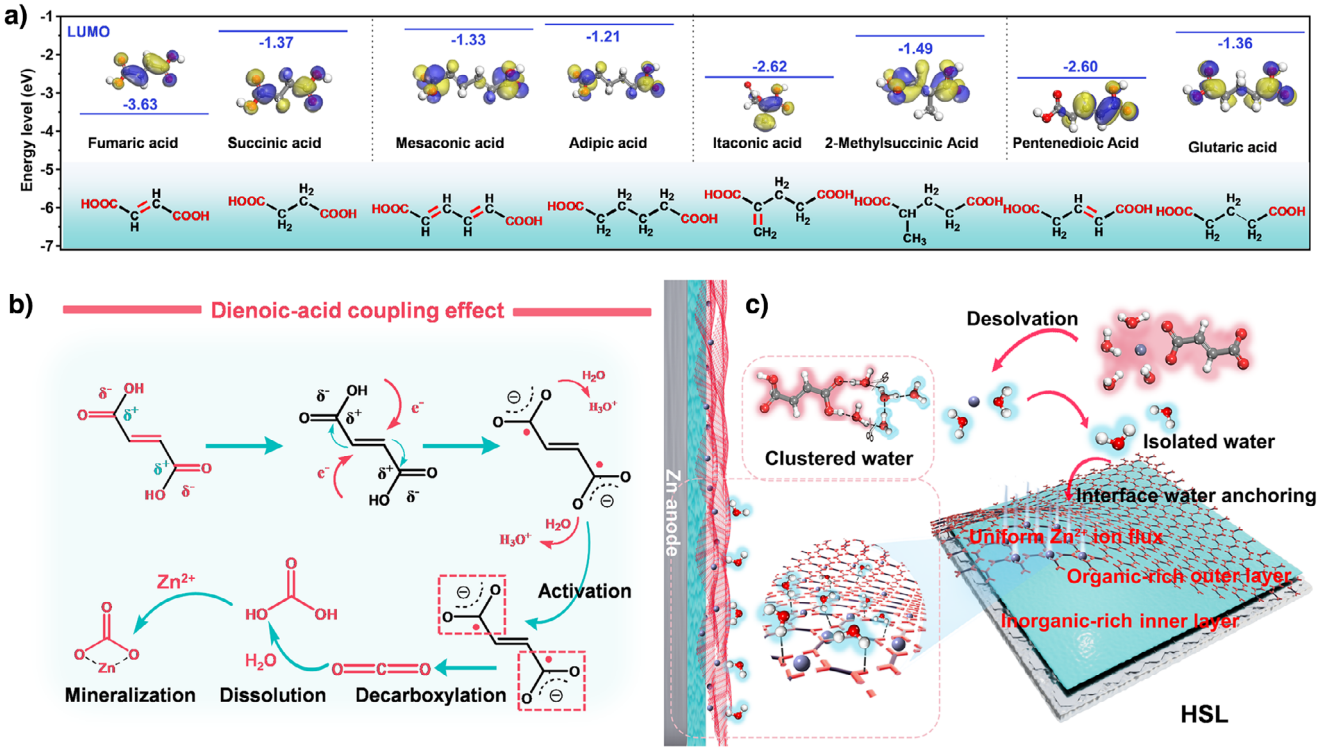

Figure 1. Schematic diagram of design methodology for hierarchical SEI via dienoic-acid coupling effect. a) The LUMO energy level comparison of organic acid with or without a double bond. b) The self-decomposition mechanism of the dienoic-acid coupling effect. c) The regulation of HSL on interfacial active H_2O and uniform deposition to suppress HER and dendrite formation for the Zn anode.

of HSL on the Zn anode. In the element mapping image (Figure S4) and FTIR spectrum (Figure S5) on Zn surface, the uniform distribution of the C element, as well as the C═O (1650 cm^{-1}) and C─O (1280 cm^{-1}) peaks further confirm the competitive adsorption behavior of FS on the electrode surface.[32] Differential capacitance (DC) (Figure S6) and electric double layer capacitance (EDLC) (Figure S7) are also adopted to investigate the adsorption and EDL on the Zn surface. The DC decrease from 116.8 to 93.3 μF cm^{-2} and the EDLC reduction from 220.21 to 76.27 μF cm^{-2} is because the larger volume of FS molecules increases the thickness of the EDL (Figure S8), leading to a significant reduction in the electrode capacitance of Zn electrolyte.[33] The surface morphology of the Zn anode with HSL remains unchanged due to the competitive adsorption behavior of FS (Figure S9), while Zn anode with ZS shows clear corrosion topography. The preferential adsorption of FS additives on the Zn surface can form strong coordination effects with Zn^{2+} ions to constitute the organic outer layer of HSL.

The chemical structure of HSL and the formation mechanism of the inorganic inner layer during cycling were investigated through transmission electron microscopy (TEM) and XPS with nanoscale depth-profiling. TEM image of HSL after cycling further demonstrate a distinct hierarchical interface on Zn anode (Figure 2c) with the outer amorphous organic adsorption layer and the inner crystalline inorganic layer with ZnS, $ZnCO_3$, and ZnO components from the self-decomposition of FS, which is also confirmed by the preferential reduction of FS over Zn^{2+} to form HSL in CV curves (Figure S10). The element mapping images of Zn^{2+} deposited Cu foil reveal a uniform distribution of C sources, substantiating uniform organic-rich layers (Figures S11 and S12). XPS spectra of the cycled Zn anode with HSL were further investigated to explore the hierarchical distribution of HSL from the outer to the inner in Figure 2d. The presence of O─C═O components (~288.4 eV) arises from the inadequate electroreduction and strong electrostatic adsorption of FS molecules in the outer SEI layer. As the etching depth increases, the organic SEI signals progressively diminish, whereas the characteristic peak of $ZnCO_3$ becomes more pronounced due to FS decomposition cause by dienoic-acid coupling effect, indicating a hierarchical distribution of organic SEI components.[34,35] In the S 2p spectrum, clear signals of SO_4^{2-} (~169.0 eV) are observed at initial etching. Subsequently, ZnS peak (~162.1 eV) formed by SO_4^{2-} is found during the subsequent etching process,[36] which is attributed to the hierarchical distribution characteristics of HSL. O 1s spectra further confirm that the organic-rich outer layer is predominantly composed of S-O or C-O at ~531.8 eV, while a new peak of ZnO or $Zn(OH)_2$ at ~530.2 eV gradually increases after post-etching.[37] Combining internal electroreduction and external adsorption of FS on the Zn surface, HSL exhibits a hierarchical distribution structure with an organic-rich outer layer and an inorganic-rich inner layer (Figure 2e). Moreover, the transport ability of Zn^{2+} in HSL was calculated by the three main components of FS, ZnS, and $ZnCO_3$ through DFT and MD simulations. The organic-rich FS outer layer possesses a high diffusion coefficient of

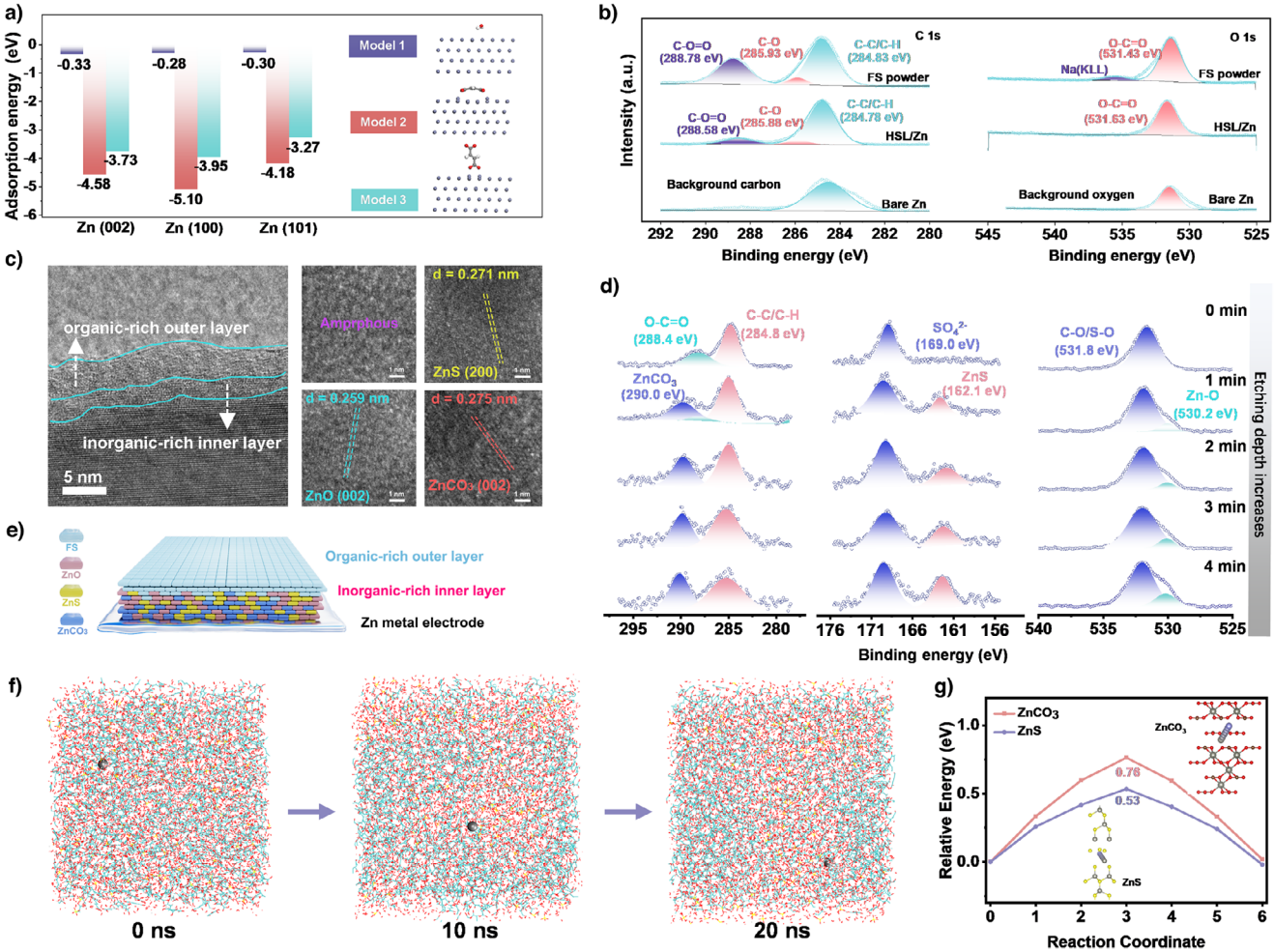

Figure 2. The formation mechanism and chemistry structure of HSL. a) The adsorption energy comparison of FS and H_2O on various Zn planes. b) The O 1s and C 1s spectra of the Zn anode immersed in ZS/FS solution. c) TEM images of HSL on the Zn surface and the corresponding lattice fringes. d) XPS spectra of C 1s, S 2p, and O 1s in HSL at different etching times. e) Schematic diagram of HSL with the hierarchical distribution. f) Zn^{2+} diffusion path simulation within the organic-rich outer layer of HSL. g) The calculated transportation energy barriers of Zn^{2+} in inorganic $ZnCO_3$ and ZnS components of HSL.

2.62×10^{-5} cm^2 s^{-1} via MD simulation to facilitate the fast ion transport (Figure 2f and Figure S13). Moreover, the inorganic-rich ZnS and $ZnCO_3$ inner layer also show low energy barriers of 0.53 and 0.76 eV (Figure 2g), respectively, which can realize the quick Zn^{2+} transportation.

The interfacial microenvironment regulation of HSL on the Zn anode was characterized and calculated via in situ experiment and theoretical calculation. The in situ surface-enhanced Raman spectroscopy (SERS) of interfacial H_2O on the Zn surface is synchronously recorded during the plating and stripping processes in Figure 3a. The characteristic peaks of H_2O on Zn anode with HSL rapidly recover as compared to those with ZS, attributed to the strong affinity and anchoring effect of the outer organic-rich HSL with H_2O. Moreover, the anchoring effect of the outer organic-rich HSL via H_2O-FS H-bonds accelerates the desolvation kinetics. The broad peak of the O–H stretching vibration (Figure 3a) is split into three Gaussian sub-bands of bulk H_2O (strong H-bonds, 3280 cm^{-1}), cluster H_2O (medium H-bonds, 3470 cm^{-1}), and isolated H_2O (weak H-bonds, 3590 cm^{-1}) in Figure S14 and 3b.[38] The increase of a strong H-bond peak on the Zn anode with ZS results in the formation of more bulk H_2O with fast proton migration to induce HER. Whereas, the more medium H-bond and less strong H-bond peaks on Zn anode with HSL derive from the anchoring effect of HSL with the dissociated H_2O molecules through the H-bond donors ($H_{FS}^{+}\cdots O_W^{-}$) and acceptors ($O_{FS}^{-}\cdots H_W^{+}$) of the organic-rich outer layer in Figure 3c, which can obstruct the proton migration path to suppress HER.[39,40] The binding energy of FS-H_2O (−0.43 eV) components are significantly stronger than the H-bond interactions of H_2O-H_2O (−0.21 eV) (Figure 3d), suggesting that H_2O molecules are more likely to bind with the outer organic HSL via stronger H-bonds and significantly reduces the activity of H_2O, as well as accelerates the dissociation process of H_2O molecules in Zn^{2+} clusters.[26] The higher binding energy of FS-Zn^{2+} (−6.86 eV) than H_2O-Zn^{2+} (−3.02 eV) implies that organic-rich outer HSL with abundant Zn affinity sites facilitates uniform Zn^{2+} flow to induce uniform Zn^{2+} deposition on the Zn anode.[41]

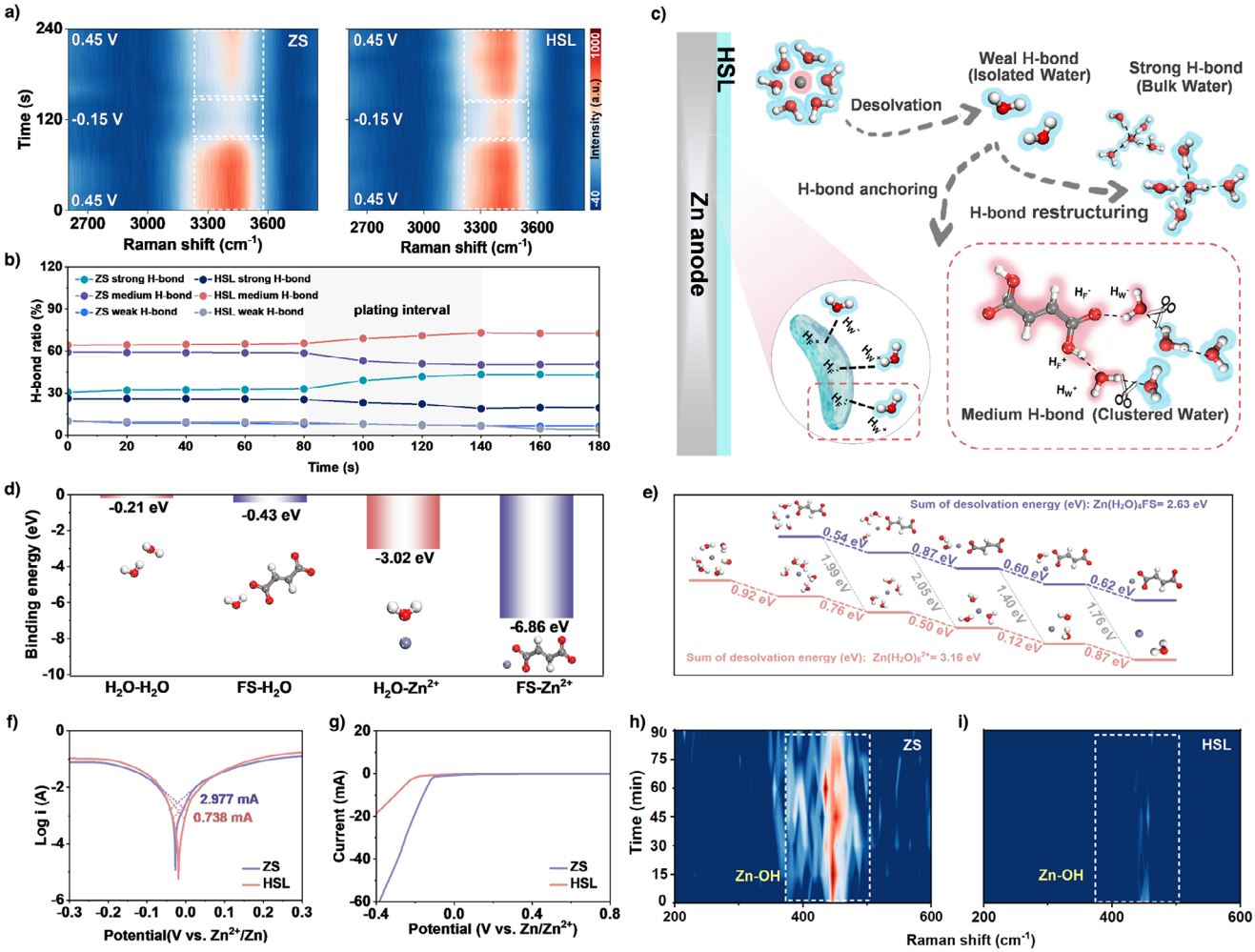

Figure 3. The regulation mechanism of HSL on interfacial H_2O. a) In situ SERS at different voltages during charge–discharge states at a scan rate of 5 mV s^{-1}. b) Proportions of strong H-bond, medium H-bond, and weak H-bond on Zn anodes with ZS and HSL during the plating process. c) Schematic diagram of H-bond regulation for HSL at the electrode/electrolyte interface. d) The binding energies of FS and H_2O with Zn^{2+} and H_2O. e) Desolvation energy of the solvated clusters in different steps for the Zn anode with ZS and HSL. f) Tafel curves of Zn anodes with ZS and HSL. g) LSV curves of ZS and HSL. h,i) In situ SERS spectra of Zn anodes with h) ZS and i) HSL during deposition processes at 5 mA cm^{-2}.

The regulation of HSL on the desolvation process was investigated by DFT to calculate the desolvation energy. The desolvation free energy calculation shows the lower energy of $Zn(H_2O)_4FS$ (-11.03 eV) compared to $Zn(H_2O)_6^{2+}$ (−9.04 eV), implying that $Zn(H_2O)_4FS$ possesses a more stable solvated structure (Figure S15). The modulation of the additive on intermolecular interaction and Zn^{2+} solvation structure in the electrolyte was verified by molecular dynamics (MD) simulations and nuclear magnetic resonance (NMR). The snapshots from MD simulations (Figure S16a) and the radial distribution function (RDF) (Figure S16b) of the corresponding Zn^{2+} show the transformation from $Zn(H_2O)_6^{2+}$ to $Zn(H_2O)_4FS$ in the Zn^{2+} solvated structure. The emergence of a new peak in HSL demonstrates the successful involvement of FS in the first solvation shell structure of Zn^{2+} ions to reduce active H_2O. The downfield shift of D_2O for HSL (Figure S17) further verifies the H-bond anchoring effect between FS and H_2O, which is beneficial for suppressing HER.[42,43] The desolvation process of $Zn(H_2O)_6^{2+}$ and $Zn(H_2O)_4FS$ (Figure 3e) is conducted to further confirm the fast desolvation kinetics. During the desolvation calculation process, each step eliminates one component (FS or H_2O) in the solvation structure. The sum of desolvation energy for $Zn(H_2O)_4FS$ (2.63 eV) is much lower than $Zn(H_2O)_6^{2+}$ (3.16 eV) due to the slightly stronger interaction of cations and anions in $Zn(H_2O)_6^{2+}$. Based on the EIS results and the Arrhenius equation, the activation energy (E_a) of charge transfer at the electrode surface is determined by fitting a linear relationship between electron transfer resistance and temperature (Figure S18). The activation energy of the Zn electrode with HSL (12.55 kJ mol^{-1}) is lower than that with ZS (22.15 kJ mol^{-1}), simultaneously demonstrating that HSL favors the desolvation kinetics and facilitates charge transfer at the electrolyte/electrode interface.[44]

The inhibition effect of HSL on HER was characterized via linear sweep voltammetry (LSV), Tafel, and in situ SERS. The lower corrosive potential (−0.027 V) and higher corrosive current (2.977 mA) of Zn anode with ZS than that with

HSL (−0.019 V and 0.738 mA) (Figure 3f) demonstrate the poor anodic corrosion tendency and corrosion rate of Zn anode with HSL. The wide electrochemical stability window of HSL compared to that of ZS (Figure 3g and Figure S19) primarily results from the strong interaction forces of FS–H_2O than H_2O–H_2O to reduce H_2O activity and hinder HER. Furthermore, in situ SERS measurements were also conducted to investigate the effect of HSL on HER-derived by-products. The parasitic $Zn(OH)_4^{2-}$ species induced by HER can be obvious observed on the Zn anode with ZS in Figure 3h, while it cannot be observed on Zn anode with HSL during the deposition process (Figure 3i), proving that HSL effectively hinders the formation of insulative by-products formed in localized alkaline environments from hydrolysis.

The hierarchical interface of HSL facilitates the uniform diffusion of Zn^{2+} ions to achieve a dendrite-free Zn anode. The surface morphology of the Zn-plated layer was characterized using optical microscopy, SEM, and in situ XRD. The plated Zn with ZS occurs significant agglomeration after deposition from 1 to 10 h in Figure 4a. Whereas, the uniform Zn electrodeposits can be observed with a dark grey appearance after the modulation of HSL on Zn anode, indicating the formation of a dense and uniform Zn layer (Figure 4b).[45] XRD patterns of the plated Zn electrodes show the characteristic peak of chemical corrosion-derived by-products on the plated Zn electrode with ZS and no obvious impure peaks on the plated Zn electrode with HSL, indicating the suppression effect of HSL on the formation of HER-derived by-products (Figure S20). In situ optical microscopy was used to dynamically observe the deposition process of Zn on the electrode surface (Figure 4c,d and Figure S21). Zn anode with ZS presents uneven deposition/stripping behavior of Zn^{2+} ion during charge/discharge processes, while Zn anode with HSL possesses the homogeneous deposition behavior and achieves a uniform plated layer. The plated Zn with ZS shows the uneven deposition morphology in Figure 4e and a loose pattern and large volume (Figure 4f), to seriously affects battery performance. Contrastingly, the plated Zn with HSL exhibits flat and dense deposition patterns (Figure 4g,h) to effectively inhibit dendrite growth, indicating that HSL with an inorganic inner layer guides the homogeneous distribution of Zn^{2+} on the electrode surface. In situ XRD shows that Zn^{2+} was deposited with a higher preference for Zn (101) throughout the deposition time, as well as a more uniform deposition pattern is favorable to delay SEI rupture due to electrode swelling (Figure 4i). In addition, no significant by-product peaks of Zn anode with HSL (Figure S22) as compared with that with ZS (Figure S23) indicate that the physical barrier and the interfacial H_2O regulation of HSL reduce the number of active H_2O to suppress HER.

The nucleation process of the Zn anode with HSL was investigated by contact angle measurements, electrochemical tests, atomic force microscopy (AFM), and finite element simulation. The contact angle of aqueous electrolyte on Zn anode with HSL (26.4°) is significantly lower than that with ZS (83°) (Figure S24) due to the affinity of the outer FS adsorption layer with H_2O molecules to facilitate the diffusion and transport of Zn^{2+} from aqueous electrolyte to electrode surface.[46] A lower exchange current density (i_0) of Zn anode with HSL (4.16 mA cm^{-2}) as compared to that with ZS (8.82 mA cm^{-2}) demonstrates a higher nucleation overpotential in the hierarchical interface, demonstrating a smaller critical nucleation radius of Zn nuclei (Figure 3j and Figure S25).[47,48] The higher nucleation overpotential of the Zn anode with HSL in cyclic voltammetry (CV) curves (Figure 4k) promotes Zn nucleation on the substrate to form a dense Zn deposition layer, thus effectively preventing the formation of Zn dendrites. The surface roughness of the deposited Zn in AFM images (Figure 4l and Figure S26) reveals that Zn^{2+} are deposited with homogeneous behavior on the Zn anode with HSL. The COMSOL simulations of the electrode surface in Figure 4m show that the Zn anode with HSL can effectively uniform the localized Zn^{2+} concentration caused by excessively high local electric field intensity to generate more compact deposition morphology for the hindrance of dendrite growth.[49]

The hierarchical interface of HSL endows the Zn anode with excellent reversibility. Zn anode with HSL exhibits stable plating/stripping performance of over 2400 cycles and maintains a high average coulombic efficiency (CE) of 99.8% (Figure 5a and Figure S27), markedly surpassing that of Zn anode with ZS electrolyte (300 cycles). The corresponding galvanostatic charge–discharge curves display the lower polarization potential (23 mV) of Zn anode with HSL over ZS (Figure 5b), suggesting that HSL effectively mitigates by-product accumulation to reduce interfacial resistance and enhance plating/stripping kinetics.[50] Moreover, Zn anode with HSL displays excellent rate performance at various current densities from 5 to 50 mA cm^{-2} (Figure 5c), demonstrating that HSL with interfacial H_2O regulation ability enhances the reaction kinetics for the plating/stripping of Zn^{2+} on Zn anode. Zn anode with HSL also shows a longer cycle life than that with ZS in the cycling-resting process (Figure 5d), illustrating that HSL can prevent electrode degradation during the intermittent operation. Zn anode with HSL can achieve a long-time cycling-life of 3800 h at 2 mA cm^{-2} (Figure 5e and S28) and possesses the low electron transfer resistance after cycling (Figure 5f) due to the synchronous regulation of HSL on solvation structure and deposition behavior. To verify the self-decomposition tendency of the dienoic-acid coupling effect, succinic acid (SA) and adipic acid (AA) are also developed as trace electrolyte additives to investigate the influence of the double bond and carbon number. Zn anodes with SA and AA exhibit a shorter cycling life of 1600 and 2200 h than that with HSL, verifying the dienoic-acid coupling effect to facilitate self-decomposition reaction for the formation of HSL on Zn anode. Zn anode with HSL still displays superior cycling stability (400 h) compared to that with ZS (30 h) (Figure 5g) at the higher current density of 10 mA cm^{-2} and deeper discharge of 10 mAh cm^{-2}, indicating the synergistic effect of hierarchical interface and active H_2O regulation to suppress HER and dendrite growth. The comparison of the electrochemical properties with the reported works in Figure 5h and Table S1 demonstrates that the Zn anode with the HSL outperforms most published works, which originates from the synchronous regulation of HSL on interfacial H_2O to suppress HER and dendrite growth.

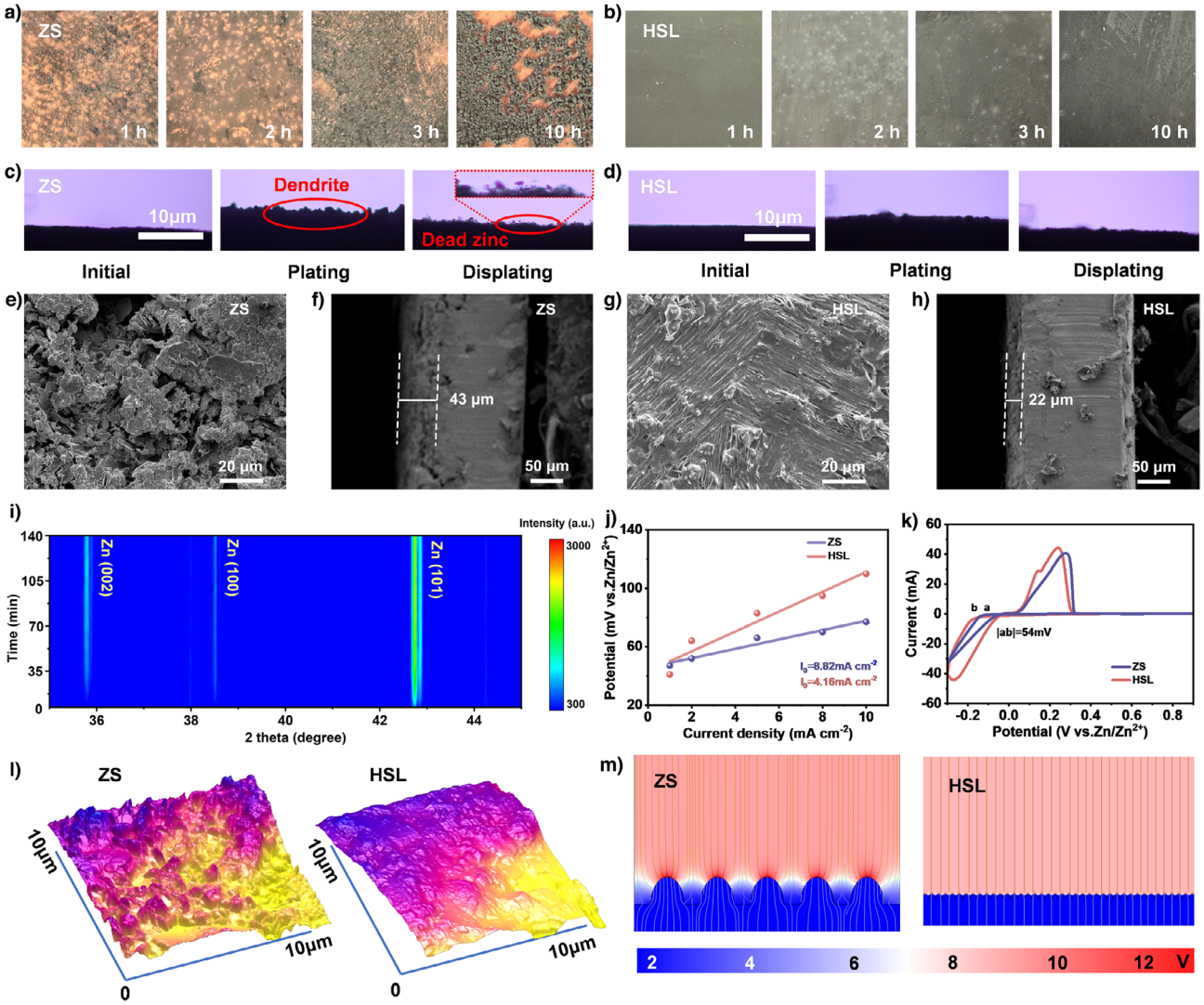

Figure 4. The regulation of HSL on deposition processes. a,b) Optical photograph of the plated Zn with a) ZS and b) HSL. c,d) In situ optical microscope photographs of Zn anodes with c) ZS and d) HSL. e–h) SEM image of Zn anodes with ZS e,f) and HSL g,h) after 20 cycles. i) In situ XRD images of Zn anode with HSL during the plating process. j) Exchange current density and k) CV curves of Zn anodes with ZS and HSL. l) AFM image of the plated Zn with ZS and HSL after 2 h at 2 mA cm^{-2}. m) The localized electric field distributions of Zn anodes with ZS and HSL.

Remarkably, Zn–I_2 battery assembled by Zn anode with HSL displays excellent electrochemical performance (Figure 6a). CV curves of the Zn–I_2 batteries with ZS and HSL in Figure 6b exhibit distinct oxidation and reduction potentials at 1.37 and 1.01 V, indicating the good redox kinetics for the Zn anode with HSL. Zn–I_2 battery with HSL possesses the higher rate performance of 130 mAh g^{-1} at 10 A g^{-1} than that with ZS (12 mAh g^{-1}) in Figure 6c. The corresponding charge/discharge curves (Figure 6d) reveal analogous charge/discharge plateaus for Zn–I_2 full battery with HSL at different current densities, further verifying its superior rate capability. Moreover, Zn–I_2 full battery with HSL achieves an impressive cycling-life of 15 000 cycles compared to that with ZS (500 cycles) (Figure 6e) at a current density of 1 A g^{-1}, resulting from the regulation of HSL on interfacial H_2O to suppress the corrosion reaction, which can be also confirmed by the flat and dense morphology of the cycled Zn anode with HSL (Figure S29) and the lower and more stable polarization potential of Zn–I_2 full battery with HSL (Figure 6f) compared to that with ZS (Figure S30). Furthermore, Zn–I_2 full battery with HSL under more practical conditions with lower E/C and N/P ratios also exhibits good cycling performance in Figure S31, resulting from the maintenance of interfacial H_2O regulation of HSL to suppress the corrosion reaction. In addition, Zn-MnO_2 battery with HSL also possesses better electrochemical performance than that with ZS (Figures S32 and S33), demonstrating the universality of HSL on aqueous Zn-based battery. The practicality of Zn–I_2 full battery with HSL was validated through the assembly of Zn–I_2 pouch battery (Figure 6g). Zn–I_2 pouch battery with HSL achieves the long cycling performance of 550 cycles (Figure 6h) at the current density of 1 A g^{-1}, superior to that with ZS (100 cycles) due to the interfacial H_2O regulation of HSL on Zn anode. Zn–I_2 pouch battery with HSL can still maintain the initial voltage at about 1.3 V at the bending and cutting states (Figure 6i) to confirm its stability

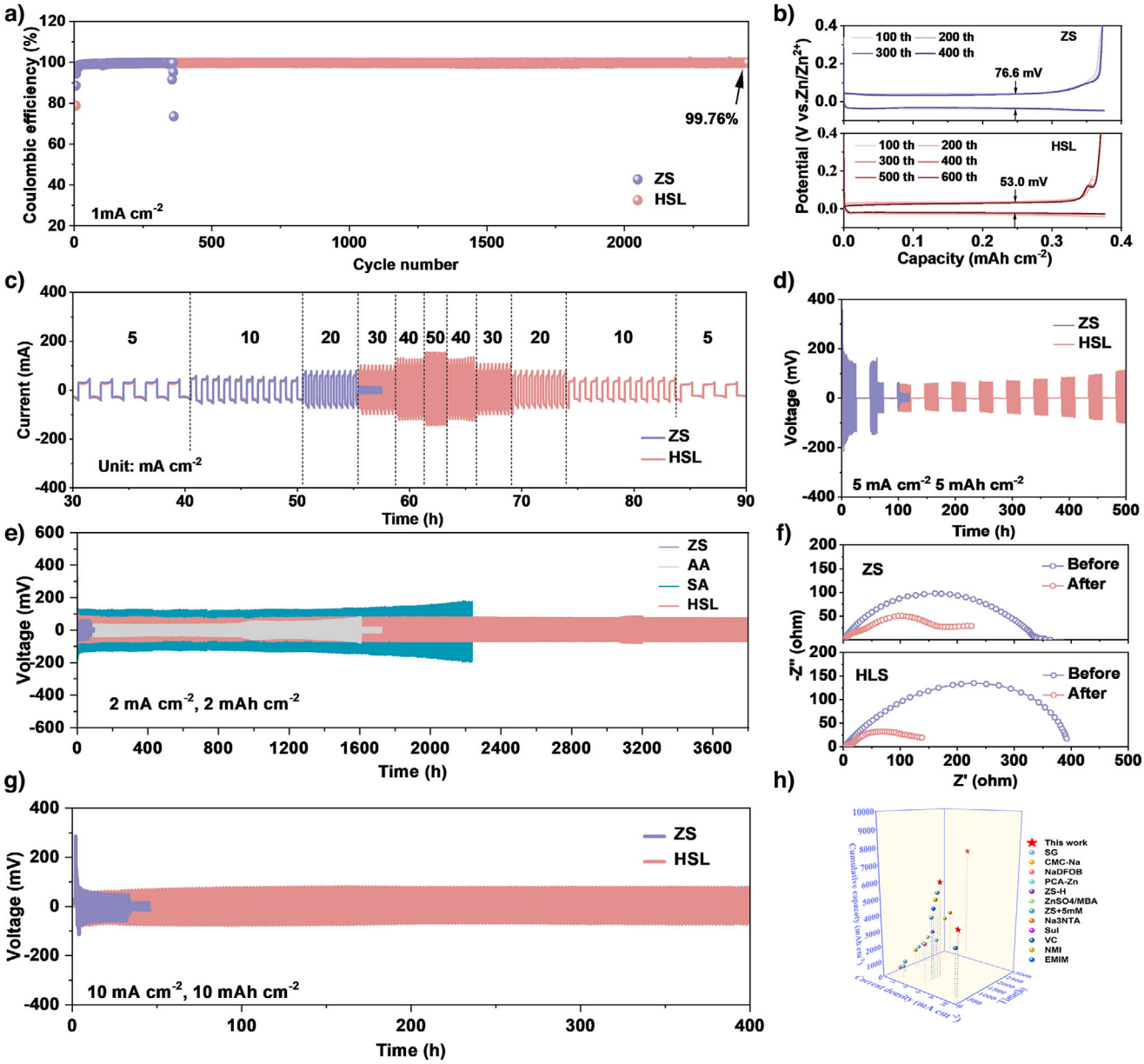

Figure 5. The electrochemical performance of the Zn anode with HSL. a) The coulombic efficiency and b) the galvanostatic charge–discharge curves of Zn anodes with ZS and HSL. c) The rate performance of Zn anodes with ZS and HSL from 5 to 50 mA cm^{-2}. d) The cycling performance of Zn anodes with ZS and HSL at 5 mA cm^{-2} for the cycling/resting interval of 24 h. e) The cycling performance of Zn anodes with ZS, AA, SA, and HSL at 2 mA cm^{-2} and 2 mAh cm^{-2}. f) EIS spectra of Zn anodes with ZS and HSL before and after 20 cycles at 2 mA cm^{-2}. g) The cycling performance of Zn anodes with ZS and HSL at 10 mA cm^{-2} and 10 mAh cm^{-2}. h) Performance comparison of this work with the previous reports.

and safety. Zn–I_2 pouch battery with HSL can also power portable instruments of LED lights, smartphone, electronic clock, and remote-control toy car, and wearable instruments of overalls (Figure 6j), confirming its practical application prospect.

Conclusion

In summary, the regulation methodology of trace additive engineering is developed to tailor a hierarchical interface and deeply reveal the self-decomposition mechanism by the dienoic acid coupling effect. As a proof of concept, trace fumarate salt (FS) additive with dual carboxyl and double bond groups is successfully employed to construct a hierarchical SEI layer (HSL) on Zn anode. Strong electron-withdrawing ability of dual carboxyl and metastable double bond facilitates the self-decomposition of FS to form the organic-rich outer layer and the inorganic-rich inner layer in HSL. The coordination effect of the organic-rich outer layer at the electrode/electrolyte interface can regulate interfacial H_2O to hinder HER and dendrite growth and facilitate the desolvation kinetics. Moreover, the inorganic-rich inner layer

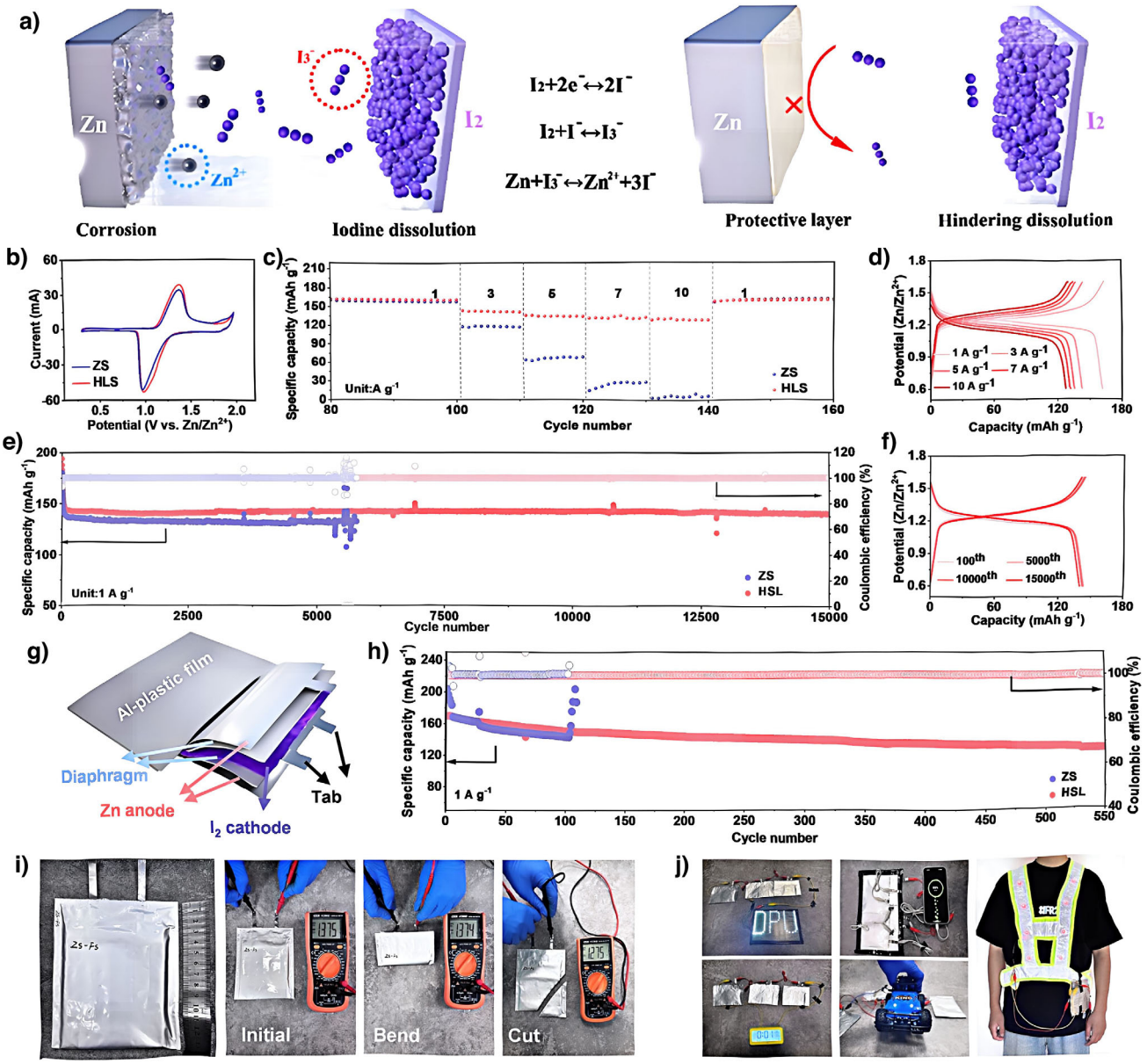

Figure 6. The electrochemical performance and practical application of Zn–I_2 full battery with HSL. a) The protective mechanism of HSL on the Zn anode of the Zn–I_2 full battery. b) CV curves of Zn–I_2 batteries with ZS and HSL. c) The rate performance and d) the corresponding charge/discharge curves of Zn–I_2 battery with ZS and HSL. e) The cycling performance and f) the corresponding charge/discharge curve of Zn–I_2 battery with ZS and HSL. g) Schematic diagram and h) cycling performance of Zn–I_2 pouch battery with ZS and HSL. i) Voltage changes of Zn–I_2 pouch battery with HSL before and after bending and cutting. j) LED lights, smartphone, electronic clock, remote-control toy car, and wearable instruments of overalls powered by Zn–I_2 pouch battery with HSL.

of HSL on the Zn surface can induce the uniform ion flux to further suppress dendrite growth. These advantages enable a Zn–Zn symmetric battery with HSL to achieve a high average coulombic efficiency of 99.8% over 2400 cycles, a long-term cycling life of 3800 h, and good reversibility under a high current density of 50 mA cm^{-2}. Moreover, Zn–I_2 full battery with HSL possesses long cycling life of 15 000 cycles at 1 A g^{-1}. This work opens a new route to design an advanced interface with fast kinetics by trace additives, which has great potential to apply to other aqueous metal-based batteries.

Acknowledgements

This work was financially supported by Dalian Science and Technology Innovation Fund Project (No. 2024JJ11PT008), the Energy Revolution S&T Program of Yulin Innovation Institute of Clean Energy (No. E411060316), the Special Fund of Basic Scientific Research Project at Undergraduate University in Liaoning Province (No. LJ212410152056), and the Foundation (No. GZKF202301) of State Key Laboratory of Biobased Material and Green Papermaking, Qilu University of Technology, Shandong Academy of Sciences.

Conflict of Interests

The authors declare no conflict of interest.

Data Availability Statement

The data that support the findings of this study are available from the corresponding author upon reasonable request.

Keywords: Aqueous zinc metal batteries · Dienoic-acid coupling · Hierarchical interface · Solid electrolyte interface

[1] D. Wang, H. Peng, S. Zhang, H. Liu, N. Wang, J. Yang, *Angew. Chem. Int. Ed.* **2023**, *62*, e202315834.
[2] C. Huang, X. Zhao, Y. Hao, Y. Yang, Y. Qian, G. Chang, Y. Zhang, Q. Tang, A. Hu, X. Chen, *Energy Environ. Sci.* **2023**, *16*, 1721–1731.
[3] L. Hong, X. Wu, Y. S. Liu, C. Yu, Y. Liu, K. Sun, C. Shen, W. Huang, Y. Zhou, J. S. Chen, K. X. Wang, *Adv. Funct. Mater.* **2023**, *33*, 2300952.
[4] K. Qi, P. Liang, S. Wei, H. Ao, X. Ding, S. Chen, Z. Fan, C. Wang, L. Song, X. Wu, C. Wu, Y. Zhu, *Energy Environ. Sci.* **2024**, *17*, 2566–2575.
[5] Y. Zhu, Z. Huang, M. Zheng, H. Chen, S. Qian, C. Sun, Y. Tian, Z. Wu, C. Lai, S. Zhang, Y. L. Zhong, *Adv. Funct. Mater.* **2024**, *34*, 2306085.
[6] P. Ruan, X. Chen, L. Qin, Y. Tang, B. Lu, Z. Zeng, S. Liang, J. Zhou, *Adv. Mater.* **2023**, *35*, 2300577.
[7] L. Jiang, D. Li, X. Xie, D. Ji, L. Li, L. Li, Z. He, B. Lu, S. Liang, J. Zhou, *Energy Storage Mater.* **2023**, *62*, 102932.
[8] Q. He, Z. Chang, Y. Zhong, S. Chai, C. Fu, S. Liang, G. Fang, A. Pan, *ACS Energy Lett.* **2023**, *8*, 5253–5263.
[9] Y. Li, X. Zheng, E. Z. Carlson, X. Xiao, X. Chi, Y. Cui, L. C. Greenburg, G. Zhang, E. Zhang, C. Liu, Y. Yang, M. S. Kim, G. Feng, P. Zhang, H. Su, X. Guan, J. Zhou, Y. Wu, Z. Xue, W. Li, M. Bajdich, Y. Cui, *Nat. Energy* **2024**, *9*, 1350–1359.
[10] T. T. Su, W. F. Ren, M. Xu, P. W. Xu, J. B. Le, X. Ji, H. Z. Dou, R. C. Sun, Z. W. Chen, *Adv. Energy Mater.* **2024**, *14*, 2401737.
[11] P. W. Xu, M. Xu, J. Zhang, J. B. Zou, Y. Shi, D. Luo, D. D. Wang, H. Z. Dou, Z. W. Chen, *Angew. Chem. Int. Ed.* **2024**, *63*, e202407909.
[12] Q. Hu, J. Hu, F. Ma, Y. Liu, L. Xu, L. Li, S. Zhang, X. Liu, J. Zhao, H. Pang, *Energy & Environ. Sci* **2024**, *17*, 2554–2565.
[13] N. Yang, Y. Gao, F. Bu, Q. Cao, J. Yang, J. Cui, Y. Wang, J. Chen, X. Liu, C. Guan, *Adv. Mater.* **2024**, *36*, 2312934.
[14] D. Wang, N. Zhang, Y. Zhang, L. Chang, H. Tang, W. Zhang, Q. Zhu, *Adv. Energy Mater.* **2025**, *15*, 2404090.
[15] J. Zheng, B. Zhang, X. Chen, W. Hao, J. Yao, J. Li, Y. Gan, X. Wang, X. Liu, Z. Wu, Y. Liu, L. Lv, L. Tao, P. Liang, X. Ji, H. Wang, H. Wan, *Nano-Micro Lett.* **2024**, *16*, 145.
[16] W. B. Tu, S. Liang, L. N. Song, X. X. Wang, G. J. Ji, J. J. Xu, *Adv. Funct. Mater.* **2024**, *34*, 2314157.
[17] T. Wang, Y. A. Wang, X. Wang, M. Chang, Y. Zhang, J. You, F. Hu, K. Zhu, *Adv. Funct. Mater.* **2024**, *15*, 2404090.
[18] G. Qu, H. Wei, S. Zhao, Y. Yang, X. Zhang, G. Chen, Z. Liu, H. Li, C. Han, *Adv. Mater.* **2024**, *36*, 2400370.
[19] X. Wang, Y. Ying, S. Chen, Q. Meng, H. Huang, L. Ma, *Nano Energy* **2024**, *119*, 109099.
[20] X. Geng, X. Hou, X. He, H. J. Fan, *Adv. Energy Mater.* **2024**, *14*, 2304094.
[21] G. Wang, H. Fu, J. Lu, S. Huang, C. Pei, D. Min, Q. Zhang, H. S. Park, *Adv. Energy Mater.* **2024**, *14*, 2303549.
[22] P. Merino, E. Marques-López, T. Tejero, R. P. Herrera, *Synthesis* **2010**, *2010*, 1–26.
[23] A. Guerrero-Corella, J. Asenjo-Pascual, T. J. Pawar, S. Díaz-Tendero, A. Martín-Sómer, *Chem. Sci.* **2019**, *10*, 4346–4351.
[24] C. Li, X. Zhang, G. Qu, S. Zhao, H. Qin, D. Li, N. Li, C. Wang, X. Xu, *Adv. Energy Mater.* **2024**, *14*,2400872.
[25] M. Sumita, K. Saito, *J. Phys. Chem. A* **2006**, *110*, 12276–12281.
[26] S. Mundle, G. Lacrampe-Couloume, B. Lollar, R. Kluger, *J. Am. Chem. Soc.* **2010**, *132*, 2430–2436.
[27] P. Xu, M. Xu, J. Zhang, J. Zou, Y. Shi, D. Luo, D. Wang, H. Dou, Z. Chen, *Angew. Chem. Int. Ed.* **2024**, *63*, e202407909.
[28] S. Wei, Z.-H. Qi, Y. Xia, S. Chen, C. Wang, Y. Wang, P. Zhang, K. Zhu, Y. Cao, X. Guo, X. Yang, Q. Cui, X. Liu, X. Wu, L. Song, *ACS Nano* **2022**, *16*, 21152–21162.
[29] T. Yan, S. Liu, J. Li, M. Tao, J. Liang, L. Du, Z. Cui, H. Song, *ACS Nano* **2024**, *18*, 3752–3762.
[30] A. D. Zapata-Loría, M. A. Pech-Canul, *Chem. Eng. Commun.* **2014**, *201*, 855–869.
[31] M. J. Bozack, Y. Zhou, S. D. Worley, *J. Chem. Phys.* **1994**, *100*, 8392–8398.
[32] V. T. Verissimo Lobo, R. W. Pacheco Ortiz, V. O. O. Gonçalves, J. Cajaiba, V. Kartnaller, *Org. Process Res. Dev.* **2020**, *24*, 988–996.
[33] J. Luo, L. Xu, Y. Zhou, T. Yan, Y. Shao, D. Yang, L. Zhang, Z. Xia, T. Wang, L. Zhang, T. Cheng, Y. Shao, *Angew. Chem. Int. Ed.* **2023**, *62*, e202302302.
[34] C. Liu, W. Xu, L. Zhang, D. Zhang, W. Xu, X. Liao, W. Chen, Y. Cao, M. C. Li, C. Mei, K. Zhao, *Angew. Chem. Int. Ed.* **2024**, *63*, e202318063.
[35] C. Lin, T. C. Li, P. Wang, Y. Xu, D. S. Li, A. Sliva, H. Y. Yang, *Small Meth.* **2024**, *8*, 2400127.
[36] Y. Liu, Y. An, L. Wu, J. Sun, F. Xiong, H. Tang, S. Chen, Y. Guo, L. Zhang, Q. An, L. Mai, *ACS Nano* **2023**, *17*, 552–560.
[37] R. Huang, J. Zhang, W. Wang, X. Wu, X. Liao, T. Lu, Y. Li, J. Chen, S. Chen, Y. Qiao, Q. Zhao, H. Wang, *Energy Environ. Sci.* **2024**, *17*, 3179–3190.
[38] W. A. Senior, W. K. Thompson, *Nature* **1965**, *205*, 170.
[39] Q. Yang, L. Guo, Z. Liu, J. Wang, H. Luo, X. Zhang, Q. He, X. Chen, M. Li, Z. Wang, Y. Jiang, R. Yuan, Z. Liu, K. Zhang, Z. Hu, Y. Huang, *Energy Storage Mater.* **2025**, *75*, 104028.
[40] P. Wang, T. Li, Y. Liu, C. Lin, Y. Cui, H. Song, B. Lu, S. Liang, H. Yang, J. Zhou, *Angew. Chem. Int. Ed.* **2025**, *64*, e202422547.
[41] L. Yang, Q. Ma, Y. Yin, D. Luo, Y. Shen, H. Dou, N. Zhu, R. Feng, Y. Kong, A. Yu, B. Cheng, X. Wang, Z. Chen, *Nano Energy* **2023**, *117*, 108799.
[42] D. Wang, D. Lv, H. Liu, S. Zhang, C. Wang, C. Wang, J. Yang, Y. Qian, *Angew. Chem. Int. Ed.* **2022**, *61*, e202212839.
[43] G. Ma, L. Miao, Y. Dong, W. Yuan, X. Nie, S. Di, Y. Wang, L. Wang, N. Zhang, *Energy Storage Mater.* **2022**, *47*, 203–210.
[44] Z. Wang, J. Diao, G. Henkelman, C. B. Mullins, *Adv. Funct. Mater.* **2024**, *34*, 2314002.
[45] W. Yuan, X. Nie, Y. Wang, X. Li, G. Ma, Y. Wang, S. Shen, N. Zhang, *ACS Nano* **2023**, *17*, 23861–23871.
[46] M. Wu, X. Wang, F. Zhang, Q. Xiang, Y. Li, J. Guo, *Energy Environ. Sci.* **2024**, *17*, 619–629.
[47] Q. Hu, J. Hu, F. Ma, Y. Liu, L. Xu, L. Li, S. Zhang, X. Liu, J. Zhao, H. Pang, *Energy Environ. Sci.* **2024**, *17*, 2554–2565.
[48] J. Li, S. Zhou, Y. Chen, X. Meng, A. Azizi, Q. He, H. Li, L. Chen, C. Han, A. Pan, *Adv. Funct. Mater.* **2023**, *33*, 2307201.
[49] Y. Ouyang, W. Zong, J. Wang, Z. Xu, L. Mo, F. Lai, Z.-L. Xu, Y.-E. Miao, T. Liu, *Energy Storage Mater.* **2021**, *42*, 68–77.
[50] K. Qiu, G. Ma, Y. Wang, M. Liu, M. Zhang, X. Li, X. Qu, W. Yuan, X. Nie, N. Zhang, *Adv. Funct. Mater.* **2024**, *34*, 2313358.

Manuscript received: June 11, 2025
Revised manuscript received: July 15, 2025
Accepted manuscript online: August 06, 2025
Version of record online: ■■, ■■